

# Tensegrity Metamaterials: Toward Failure-Resistant Engineering Systems through Delocalized Deformation

Jens Bauer, Julie A. Kraus, Cameron Crook, Julian J. Rimoli,\* and Lorenzo Valdevit\*

Failure of materials and structures is inherently linked to localized mechanisms, from shear banding in metals, to crack propagation in ceramics and collapse of space-trusses after buckling of individual struts. In lightweight structures, localized deformation causes catastrophic failure, limiting their application to small strain regimes. To ensure robustness under real-world nonlinear loading scenarios, oversized linear-elastic constructions are adopted. Here, the concept of delocalized deformation as a pathway to failure-resistant structures and materials is introduced. Space-tileable tensegrity metamaterials achieving delocalized deformation via the discontinuity of their compression members are presented. Unprecedented failure resistance is shown, with up to 25-fold enhancement in deformability and orders of magnitude increased energy absorption capability without failure over same-strength state-of-the-art lattice architectures. This study provides important groundwork for design of superior engineering systems, from reusable impact protection systems to adaptive load-bearing structures.

Failure of materials and structures, including ductile metals, brittle ceramics, discrete foams and space-trusses, is typically preceded by highly localized deformation. Formation of shear bands and crack surfaces, and buckling of walls and struts thereby cause a chain reaction of locally confined damage events, while large parts of the system do not experience critical loads. Breaking with this established paradigm, we present 3D tensegrity metamaterials which delocalize deformation, demonstrating a pathway toward superior failure-resistant load bearing systems (Figure 1).

In load-bearing systems, localized deformation translates into system-level instability, i.e., a decrease in load bearing capacity with increasing deformation, entailing deformation

bursts without further load increase until forces are balanced again (often after a catastrophic collapse). Likewise, system-level instability is an indication of localized deformation. In contrast, a system is stable when increasing deformation leads to increased load bearing capacity. From a system's stress-strain response, the first occurrence of a negative stiffness event identifies unstable deformation. A stable stress-strain response is free from negative stiffness events and shows a monotonic relationship between increasing stress and strain.

Lightweight structural design, like in truss-lattices, is considered fundamentally tied to early failure from unstable deformation, strongly narrowing its applicability to mostly linear elastic, small strain scenarios. When elastically loaded, the

members of stretching-dominated lattice designs predominantly experience uniaxial tension or compression, uniformly utilizing the constituent material. This can grant 100 times higher elastic strength and stiffness over bending-dominated structures like foams, where members predominantly experience bending.<sup>[1]</sup> However, this gain implies unstable post-yield deformation, such as buckling and brittle collapse.<sup>[1,2]</sup> Thus, established stretching-dominated designs suffer from characteristic instability, inevitably resulting in catastrophic failure when structures are loaded beyond an initial peak strength. Over the past decades, lattice structures have grown into the burgeoning field of architected metamaterials, i.e., periodic networks of lattice members with combinations of effective properties unobtainable by monolithic solids.<sup>[3,4]</sup> Novel materials for additive manufacturing,<sup>[5,6]</sup> hierarchical architectures,<sup>[7,8]</sup> shell-designs,<sup>[9–11]</sup> and miniaturization of lattice members to exploit pronounced nanoscale material size-effects,<sup>[12,13]</sup> demonstrated ever higher strengths and stiffnesses. Yet these novel metamaterials are still plagued by the same localized failure phenomena that affect monolithic solids. Although deformability to high compressive strains and subsequent recoverability have repeatedly been shown under displacement-controlled laboratory conditions,<sup>[7–9,12–20]</sup> deformations remained highly localized, inherently unstable, and characterized by layer-by-layer collapse. In a load-controlled environment, which represents the vast majority of real-life situations, all these materials would experience catastrophic failure with a complete collapse following the first negative stiffness event. The lack of a stable large-strain deformation regime still restricts applications of lattice structures. To this day, nonlinear, dynamic load scenarios,

Dr. J. Bauer, Prof. L. Valdevit  
Mechanical and Aerospace Engineering Department  
University of California  
Irvine, CA 92697, USA  
E-mail: valdevit@uci.edu

J. A. Kraus, Prof. J. J. Rimoli  
School of Aerospace Engineering  
Georgia Institute of Technology  
Atlanta, GA 30332, USA  
E-mail: julian.rimoli@aerospace.gatech.edu

C. Crook, Prof. L. Valdevit  
Materials Science and Engineering Department  
University of California  
Irvine, CA 92697, USA

 The ORCID identification number(s) for the author(s) of this article can be found under <https://doi.org/10.1002/adma.202005647>.

DOI: 10.1002/adma.202005647

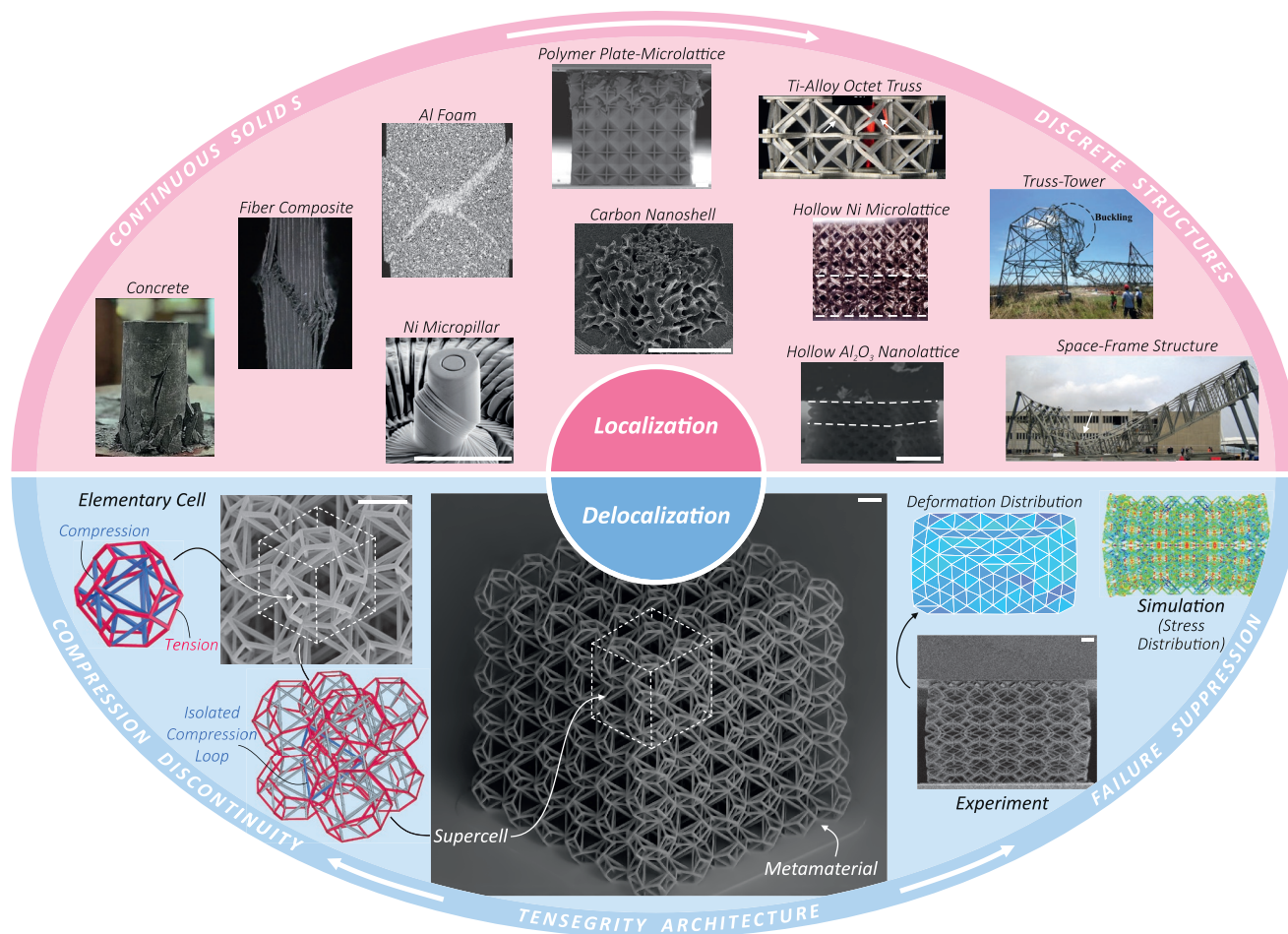


**Figure 1.** Failure resistance through delocalized deformation-tensegrity metamaterials as a pathway. (Top) Independent from the underlying mechanisms, examples of localized deformation and failure can be found across different classes of continuous solids<sup>[33–36]</sup> and discrete structures.<sup>[13,14,16,19,20,37,38]</sup> (Bottom) Structural hierarchy of a tensegrity metamaterial and its ability to delocalize deformation. Recursive reflection of a truncated octahedron elementary cell creates space-tiling  $2 \times 2 \times 2$ -cell supercells with isolated compressive member loops that do not form continuous paths which extend through the  $6 \times 6 \times 6$ -cell metamaterial. Characteristic measured and simulated uniaxial compression behavior; compression discontinuity prevents localized failure propagation and enables the metamaterial to achieve a homogeneous, delocalized deformation distribution. All scale bars are  $10 \mu\text{m}$ . “Concrete” image: Reproduced under the terms of the CC-BY Creative Commons Attribution 4.0 International license (<https://creativecommons.org/licenses/by/4.0>).<sup>[33]</sup> Copyright 2020, The Authors, published by Springer Nature. “Fiber Composite” image: Reproduced with permission.<sup>[34]</sup> Copyright 2020, Dr. R. Blows, R-TECH Materials, Swansea University. “Ni Micropillar” image: Reproduced with permission.<sup>[35]</sup> Copyright 2005, Elsevier. “Al Foam” image: Reproduced with permission.<sup>[36]</sup> Copyright 2005, Elsevier. “Polymer Plate-Microlattice” image: Reproduced under the terms of the CC-BY Creative Commons Attribution 4.0 International license (<https://creativecommons.org/licenses/by/4.0>).<sup>[13]</sup> Copyright 2020, The Authors, published by Springer Nature. “Carbon Nanoshell” image: Reproduced with permission.<sup>[16]</sup> Copyright 2019, Wiley-VCH. “Ti-Alloy Octet Truss” image: Reproduced with permission.<sup>[19]</sup> Copyright 2015, Elsevier. “Hollow Ni Microlattice” image: Reproduced with permission.<sup>[20]</sup> Copyright 2011, AAAS. “Hollow  $\text{Al}_2\text{O}_3$  Nanolattice” image: Reproduced with permission.<sup>[14]</sup> Copyright 2014, AAAS. “Truss-Tower” image: Reproduced with permission.<sup>[37]</sup> Copyright 2018, Elsevier. “Space-Frame Structure” image: Reproduced with permission.<sup>[38]</sup> Copyright 2011, ASCE.

from inertia forces in vehicle bodies to aerodynamic loads on wind turbine blades,<sup>[21]</sup> are inefficiently accommodated by linear-elastic designs, which need to be endowed with generous safety factors to prevent catastrophic failure under rarely occurring extreme loads. Impact protection systems (e.g., helmet padding), which must undergo extensive deformation in order to absorb energy, require application of inefficient foam materials to ensure stable stress–strain behavior.<sup>[2]</sup>

Tensegrity structures are lightweight trusses whose internal load-transfer mechanisms and deformation intrinsically differ from those of other lattice topologies. All established lattice architectures are continuous compression designs, meaning

that when subjected to external loading their internal stress distribution contains uninterrupted paths of connected compressive members extending throughout the structure. In contrast, tensegrities are composed of discontinuous compressive members, isolated from one another and only connected through a continuous network of tensile members.<sup>[22,23]</sup> Biological load-bearing structures, from the cytoskeleton of individual cells to the human spine, efficiently utilize tensegrity designs.<sup>[24,25]</sup> Although the tensegrity concept was discovered a century ago, the complexity of form finding techniques has until recently restricted man-made tensegrity constructions to certain low-dimensional objects, like columns and plates.<sup>[26,27]</sup> Today,

applications are largely limited to art installations, whereas technical utilization is comparably scarce and, as with all trusses, limited to linear elastic cases.<sup>[25,27,28]</sup> Despite the unique isolation of compression members, the non-linear deformation and damage behavior of tensegrities is largely unknown.

In this work, space-tileable 3D tensegrity metamaterials were constructed via recursive reflection of truncated octahedron elementary cells,<sup>[26]</sup> and 3D-printed by two-photon polymerization direct laser writing (TPP-DLW) (Figure 1). The truncated octahedron cells were composed of tensile members (red) along the polyhedron edges and compressive members (blue) inside the cell. This elementary cell itself cannot be space-tiled as the oppositely twisted square faces would not overlap. However, recursive reflection creates an 8-unit supercell with coinciding nodes on the faces of the containing cube, forming the building block for the 3D tensegrity metamaterial (Figure S1, Supporting Information). Satisfying the tensegrity definition of Fuller and Pugh in 3D space,<sup>[22,23]</sup> the compressive members of the final structure do not form continuous compression paths extending throughout the structure, but only discontinuous closed loops isolated from one another and exclusively connected through the continuous network of tensile members. Tensegrity specimens with 4–12% relative density,  $\bar{\rho}$ , i.e., the volume fraction of the solid material, were printed with  $6 \times 6 \times 6$  elementary cells. All truss members were designed as square-shaped bars with  $\approx 950$  nm average edge length; elementary cell sizes of 10–20  $\mu\text{m}$  controlled the desired relative densities. For comparison, octet truss and Kelvin foam specimens were fabricated under identical conditions as the tensegrity metamaterials. The octet architecture was chosen as the most well-established implementation of a stretching-dominated continuous-compression design. The Kelvin foam represents a bending-dominated architecture similar to the tensegrity topology, albeit without the compressive members.

Figure 2a compares the deformation behavior under displacement-controlled uniaxial compression of the tensegrity metamaterial, the octet architecture, and the Kelvin foam at 4% relative density. In situ still frames and displacement maps show the inner-specimen deformation distribution at the indicated points of the stress–strain responses. The deformation distribution was measured as the map element areas,  $a$ , relative to their undeformed initial areas,  $a_0$  (see the Experimental Section), as determined via digital image correlation (DIC) tracking of the lattice nodes from the in situ images. To quantify the resistance of the cellular architectures against localized deformation, we introduce the delocalization efficiency,  $\eta_d$ , calculated as the function

$$\eta_d = 1 - \frac{\text{std}(a/a_0)}{\text{std}_{\max}(i_t)} \quad (1)$$

with the standard deviation,  $\text{std}(a/a_0)$ , of the deformation map element areas,  $a/a_0$ , and the theoretical maximum standard deviation,  $\text{std}_{\max}(i_t)$  based on the total number of elements,  $i_t$  (see the Experimental Section).  $\eta_d = 1$  corresponds to maximum delocalization with a completely uniform deformation distribution, and  $\eta_d = 0$  represents localization with the highest possible standard deviation. For strains,  $\varepsilon$ , above 30%, reliable deformation mapping was complicated by the increasing compaction of the specimens. However, during densification in the high-strain-regime,  $\eta_d$  approaches 100% independently on the specimen.

Whereas the tensegrity metamaterial delocalized deformation mechanisms, the octet and Kelvin deformations were highly localized, with strongly confined damage events (Figure 2a). At any given time, the deformation distribution within the tensegrity was highly uniform, and largely independent of the applied strain (Movie S1, Supporting Information). Strain energy was evenly distributed within the material, and after 30% strain, no detectable localized damage was found in either the elementary cells or individual bars. In fact, in situ images did not show any notable localization until complete densification (Movie S1, Supporting Information). By contrast, the octet architecture showed a characteristic inhomogeneous layer-by-layer deformation pattern (Movie S2, Supporting Information). Strains in excess of  $\varepsilon = 2.6\%$  induced localized damage, including fracture and plastic warping of individual bars, which concentrated most of the strain energy. At  $\varepsilon = 30\%$ , about one third of the octet structure was heavily deformed and partially fractured, while the rest of the specimen was largely undeformed. Despite initially uniform deformation, the Kelvin foam suffered severe shear-type localization above  $\varepsilon = 17\%$ , accompanied by plastic warping and fracture events (Movie S3, Supporting Information).

Compared to the octet and Kelvin architectures, the tensegrity metamaterial had a fully stable stress–strain response, with a continuous monotonic stress increase with increasing strain, and a smooth, elongated post-yield plateau before densification above  $\varepsilon = 62.5\%$ . The stress–strain responses of the octet and Kelvin architectures were largely unstable, with increasing strain often causing pronounced negative stiffness events, implying a decrease of the structures' load bearing capability. Strains as low as  $\varepsilon = 2.6\%$  caused the octet to undergo system-level instability, with catastrophic failure-inducing stress drops. The bending-dominated Kelvin foam retained stable behavior beyond the linear elastic regime, however, at  $\varepsilon = 17\%$  instability, as found for the octet architecture, set in as well.

Comparison of the stress–strain responses and delocalization efficiency curves, which were derived from the deformation maps, showed the absence of system-level instability directly correlated to delocalized deformation. Consistent with its fully stable response, the tensegrity metamaterial maintained delocalization efficiencies above  $\eta_d = 90\%$  throughout the experiment, with only minor dependency on the applied strain. In contrast, the octet architecture's  $\eta_d$  values dropped to only 35% as the applied strain increased. Similarly,  $\eta_d$  of the Kelvin foam decreased to 67% during shear localization. For both architectures, the points of most rapidly increasing localization thereby occurred in the immediate proximity of the most prominent instability events in the stress–strain behaviors, such as the stress drop in the Kelvin foam response at  $\varepsilon = 17\%$ .

Figure 2b–d shows that the deformation behaviors described above for the 4%-tensegrity, -octet, and -Kelvin specimens well translated to 8% and 12% relative density, respectively. Independent of increasing relative density, the tensegrity metamaterial maintained delocalized deformation and fully stable stress–strain responses with  $\eta_d$  values largely above 90% throughout the experiments. Likewise, the octet and Kelvin specimens showed highly localized deformation and unstable stress–strain responses at  $\bar{\rho} > 4\%$ , with catastrophic failure-inducing stress drops correlating with rapidly decreasing delocalization efficiency curves (Movies S4–S9, Supporting Information).

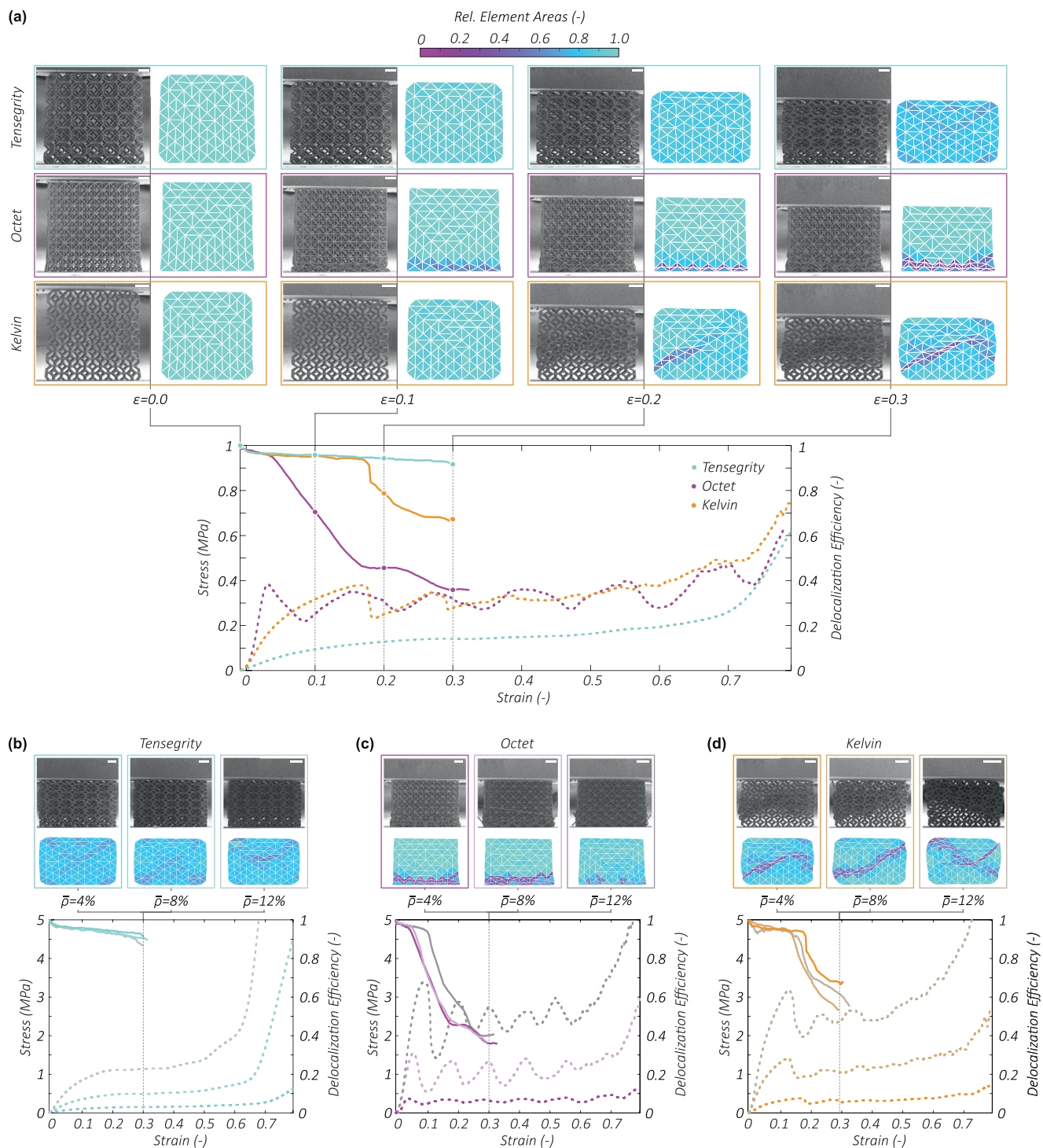


**Figure 2.** In contrast with both established stretching- and bending-dominated architectures, tensegrity metamaterials delocalize deformation. a) Uniaxial compression of 4%-relative density tensegrity, octet, and Kelvin specimens. In situ still frames and corresponding deformation maps show that independently of the applied strain,  $\epsilon$ , the tensegrity metamaterial maintains a highly uniform delocalized deformation distribution, consistent with a fully stable stress–strain response. Octet and Kelvin deformations are highly localized, with strongly confined damage events. Stress–strain responses and delocalization efficiency curves, which are derived from the deformation maps, show failure from system-level instability directly correlated to localized deformation. b–d) Comparison of experiments at 4%, 8%, and 12% relative density,  $\bar{\rho}$ , with the tensegrity (b), octet (c), and Kelvin (d) specimens demonstrate that the qualitative deformation and mechanical behaviors are consistent across different densities. All scale bars are 10  $\mu\text{m}$ .

To measure the damage resistance during delocalized and localized deformation, we performed displacement-controlled uniaxial compressive loading–unloading cycles

with progressively increasing cycle strain,  $\epsilon_c$  (5%, 10%, ..., 90%), with 4%-relative density tensegrity, and octet specimens (Figure 3). As under monotonic loading, the tensegrity

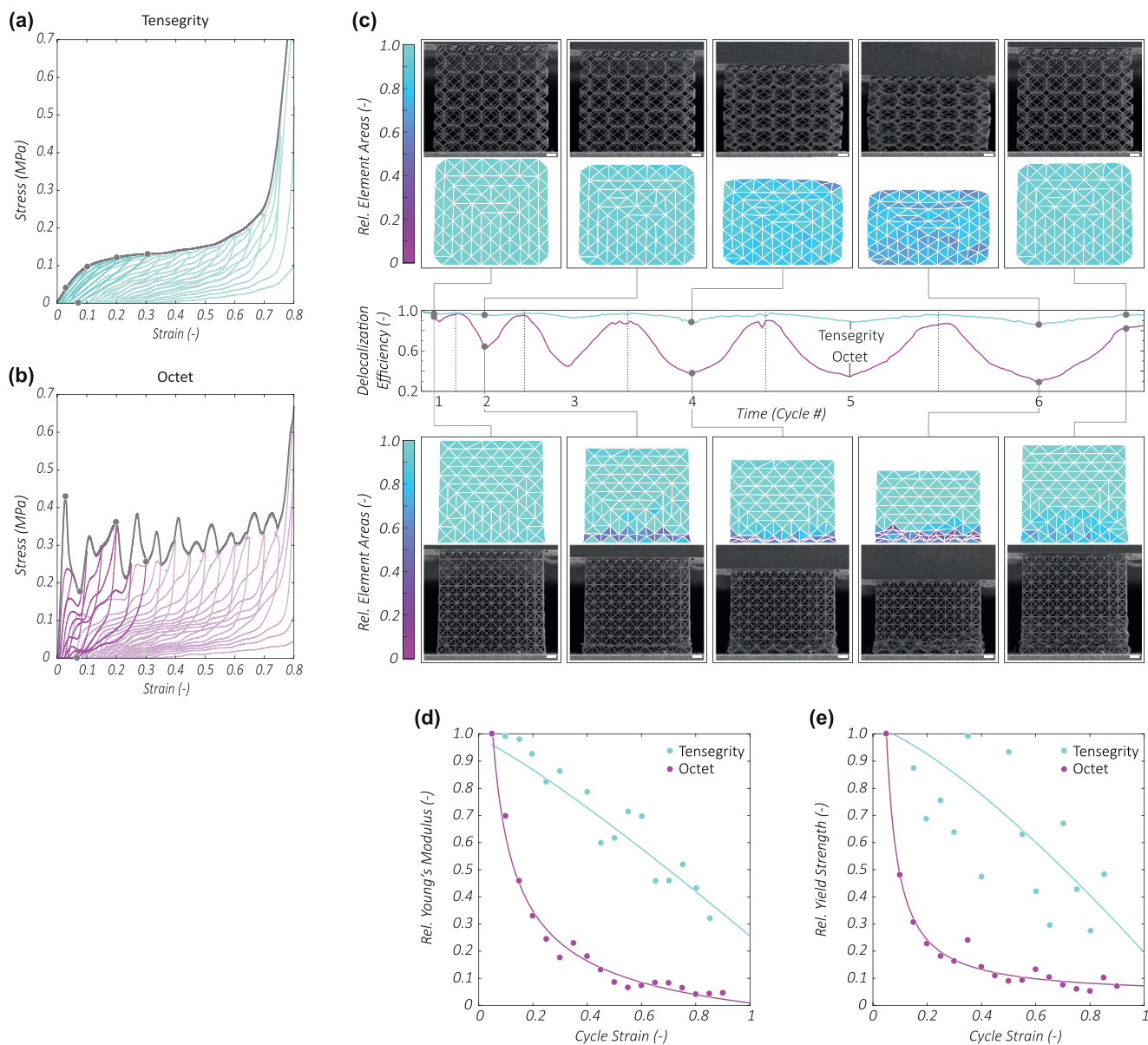


**Figure 3.** Tensegrity metamaterials resist damage through delocalized deformation. a,b) Stable and unstable stress–strain behavior of a tensegrity (a) and an octet specimen (b), respectively, under cyclic loading–unloading with progressively increasing cycle strain. Monotonic envelopes are shown in gray, highlighted cycles and marked points correspond to the deformation data in (c). c) Experiment still frames, deformation maps and delocalization efficiency–time curves show delocalized deformation without noticeable damage for the tensegrity specimen versus highly localized deformation with severe warping and fracture in the octet specimen. Scale bars are 10  $\mu\text{m}$ . d,e) Progressions of Young's modulus (d) and yield strength (e) relative to the first-cycle-values show drastically enhanced property retention consistent with stable, delocalized deformation. Measured data points and power-law fits.

metamaterial had a fully stable stress–strain behavior throughout each loading–unloading cycle (Figure 3a). The octet response was largely unstable, with stress drops occurring at the same characteristic strains within the different cycles (Figure 3b). Figure 3c compares the delocalization efficiency and the corresponding deformation distributions within the two architectures at different stages of the first six loading–unloading cycles (up to 30% strain). Largely maintaining  $\eta_d$  values above 90%, the tensegrity's delocalized deformation behavior was notably unaffected by previous loading cycles (Movies S10 and S11, Supporting Information). After 6 loading–unloading cycles up to 30% strain, no detectable localized damage was found in either the elementary cells

or individual bars. By contrast, the octet architecture showed a characteristic, localized layer-by-layer deformation pattern throughout all loading–unloading cycles with  $\eta_d$  values down to 29% (Movies S12 and S13, Supporting Information). After 6 cycles up to 30% strain, about one third of the octet structure remained heavily deformed and partially fractured, while the rest of the specimen was largely undeformed.

Delocalized deformation provided the tensegrity metamaterial an order of magnitude higher damage resistance than the localizing octet architecture. The damage resistance was determined by the evolution of the elastic properties with the progressively increasing cycle strain,  $\epsilon_c$ . Figure 3d,e shows how localized and delocalized deformation affected stiffness and

yield strength as a function of  $\varepsilon_c$ . Consistent with localized deformation, the octet architecture's elastic properties rapidly degraded under further applied strain. Increasing  $\varepsilon_c$  by 10% with respect to the first cycle caused a 55% and a 70% stiffness and yield strength knockdown, respectively. At the same time, the tensegrity metamaterial retained about 98% and 90% of the initial stiffness and yield strength, respectively, consistent with the delocalized deformation discussed above. For larger  $\varepsilon_c$ , the octet performance dropped to less than 10% of the initial values, whereas the tensegrity metamaterial retained properties notably better. At  $\varepsilon_c = 70\%$ , the octet had only 7% of its initial stiffness compared to the tensegrity's 70%. For the yield strength, similar relations were found, albeit with higher scatter. In absolute terms, the initial octet yield strength and stiffness were about 9 and 14 times higher than the corresponding tensegrity properties. As the octet properties dropped much faster with increasing strain, both architectures reached comparable values for  $\varepsilon_c$  above  $\approx 45\%$  (Figure S2, Supporting Information).

Damage resistance stemming from delocalized deformation granted our tensegrity metamaterials superior deformability and energy absorption before failure over continuous-compression architectures with the same density and strength. Figure 4a–c compares the measured monotonic compressive stress–strain

responses of the 4%-relative density tensegrity, octet, and Kelvin structures. For a realistic assessment, failure must thereby be considered as the onset of instability, although the displacement-controlled characterization performed herein allowed controlled observation of large-strain deformations with regions of negative stiffness without catastrophic collapse. The octet and Kelvin specimens failed at  $\varepsilon = 2.6\%$  and  $\varepsilon = 17\%$ , respectively. In contrast, the tensegrity metamaterial retained its load-bearing capacity until complete densification, which began at  $\varepsilon = 62.5\%$ , marking a 22 and 4 times increase in deformability without failure compared to the octet and Kelvin structures, respectively. Thereby, the tensegrity absorbed about 13 and 2 times as much energy as the octet and Kelvin architectures, respectively (Figure 3d), with the strain energy,  $U$ , given by the area under the corresponding stress–strain curves up to either failure or densification, whichever occurred first. The plateau strength,  $\sigma_p$ , and the stiffness,  $E$ , of the tensegrity reached about 37% of the maximum strengths,  $\sigma_m$ , of the octet and Kelvin specimens and less than 10% and 30% of their stiffness, respectively.

We complemented our experimental efforts with finite element simulations, which accurately reproduced our measurements. Figure 4a–c compares the computed compressive stress–strain behavior to the measured responses of the

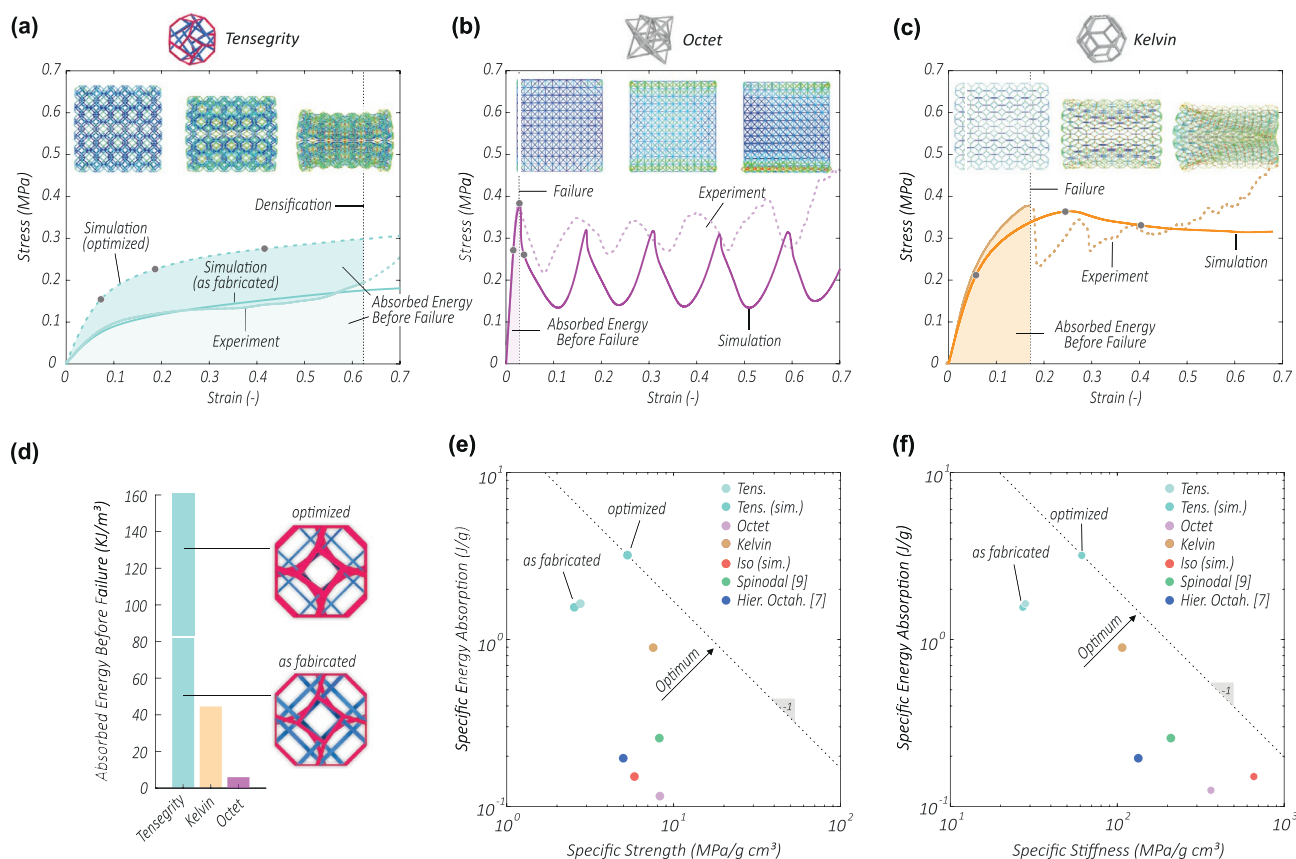


**Figure 4.** Tensegrity metamaterials achieve superior deformability and energy absorption capability without failure, over same-density and same-strength continuous-compression architectures. a–c) Experimentally measured and finite element simulated compressive stress–strain responses of same density,  $\bar{\rho} = 4\%$ , tensegrity (a), octet (b), and Kelvin (c) architectures. Insets show the computed deformation and stress distribution at the indicated strains. d) Absorbed strain energy before failure. e,f) Experimentally measured and simulated (sim.) specific energy absorption versus specific strength (e) and specific stiffness (f). Tensegrity simulations include as-fabricated model and a configuration with optimized ratio of tension to compression member cross-section dimension.

4%-relative density tensegrity, octet and Kelvin structures. The tensegrity simulation closely captured the experimentally measured behavior, where the fully stable stress–strain response was, as in the experiment, consistent with delocalized deformation (Movie S14, Supporting Information). Octet and Kelvin simulations confirmed pronounced localization coinciding with unstable stress drops, in good qualitative agreement with the experiments (Movies S15 and S16, Supporting Information). Unlike experiments, simulations were not subjected to effects such as physical contact of lattice members, resulting in a certain quantitative deviation between computed and experimentally measured stress in the post-yield regime.

Furthermore, our computational model showed that numerical optimization can drastically improve the tensegrity metamaterial's mechanical properties with respect to as-fabricated specimens, while retaining delocalized deformation behavior and damage resistance (Figure 4a,d and Movie S17, Supporting Information). Tensegrity topologies explicitly define which members experience tension and which compression. This assignment remains the same for any load case, allowing optimization of the cross-sections of tensile and compressive members' dimensional ratios without inducing anisotropy. The same cannot be done with continuous-compression architectures, where members are loaded in tension for one load case and in compression for another and vice versa. Parametric numerical optimization of tensegrity models revealed that a  $\approx 40\%$  increase and a  $\approx 48\%$  reduction of the tensile and compressive member cross-sectional dimensions, respectively, maximized the stress–strain response over the as-fabricated configuration, while maintaining the same deformation behavior and the same relative density of  $\bar{\rho} = 4\%$ . The mechanical properties of this optimized tensegrity configuration approximately doubled with respect to the fabricated structure, reaching about 70% of the octet and Kelvin peak strengths and 20% and 60% of their respective stiffnesses. Simultaneously, the absorbed strain energy before failure increased to 26 and 4 times the values of the experimentally characterized octet and Kelvin specimens.

Figure 4e,f compares specific energy absorption capability,  $\bar{U} = U / \rho$ , specific strength,  $\bar{\sigma} = \sigma / \rho$ , and specific stiffness,  $\bar{E} = E / \rho$ , of the 4% relative density samples in this study, as well as literature-reported experimental data. For a meaningful comparison, all literature data corresponded to 2–5%-relative density structures which were 3D-printed via TPP-DLW from the same polymer as the specimens in this study, and specific properties were used to accommodate for the slightly different relative densities. Strength values corresponded to the plateau strength or the maximum strength before failure, whichever applied. Reaching 3–18 and 2–7 times higher combinations of  $\bar{\sigma}$  and  $\bar{U}$ , and  $\bar{E}$  and  $\bar{U}$ , respectively, our numerically optimized tensegrity metamaterial was computed to outperform both the stretching- and bending-dominated first-order beam lattices of this study, as well as advanced hierarchical and shell-based architectures reported in the literature.<sup>[7,9]</sup> The experimentally characterized tensegrity configuration still achieved comparable combinations of  $\bar{E}$  and  $\bar{U}$  as the other architectures, and had up to 5 times higher combinations of  $\bar{\sigma}$  and  $\bar{U}$ , with only the Kelvin foam achieving a 30% higher values. Literature reported hierarchical third-order octahedron lattices and spinodal shell-architectures fell in between the first-order octet and Kelvin

lattices of this study, with their post-yield deformation reportedly still being localized and unstable.<sup>[7,9]</sup> Via finite element simulations, we further extended comparison to include the iso truss, a fully isotropic stretching-dominated continuous compression beam lattice,<sup>[10]</sup> whose deformation and mechanical behavior was found similar to that of the octet structure, albeit with lower strength and higher stiffness (Figure S3 and Movie S18, Supporting Information).

While the strengths of the tensegrity metamaterial configurations and comparison structures studied here were of the same order of magnitude, differences in energy absorption capability before failure and stiffness were more drastic and inversely correlated (Figure 4e,f). Decreasing relative density was found to amplify this effect. Our computational approach extended comparison below the experimental fabrication limit of  $\bar{\rho} \approx 4\%$  down to  $\bar{\rho} \approx 0.5\%$  (Movies S19–S33, Supporting Information), hence capturing a density regime that is inaccessible with the applied manufacturing approach. Figure S4, Supporting Information, compares the experimentally measured and computed strength, stiffness, and energy absorption before failure, as a function of the relative density. As  $\bar{\rho}$  was decreased from 4% to 0.5%, the stiffness of the as-fabricated tensegrity configuration was computed to decrease from above 7% of the corresponding octet value to less than 3%. However, at the same time the absorbed energy before failure increased to 225 times of that of the octet. In contrast, the highest experimentally measured tensegrity with a relative density of  $\bar{\rho} = 12\%$  reached about 20% of the octet's stiffness and absorbed  $\approx 3$  times as much energy before failure. Independent of  $\bar{\rho}$ , the strength ratios of the comparison architectures remained comparable to those of  $\bar{\rho} = 4\%$  (Figure 4).

In this study, we demonstrated that tensegrity architectures suppress localized deformation and damage events, a phenomenon that we attribute to the unique discontinuity of their compressive members. In a tensegrity architecture, instability of a compressive member can only propagate through tensile load paths, which, contrary to compressive members, cannot experience instability, provided they do not rupture. Hence, the propagation of an instability is suppressed, preventing localized deformation. In contrast, we showed that the distinctive premature compressive failure of state-of-the-art lattice designs directly correlates with their highly localized deformation mechanisms. These mechanisms relate to the presence of continuous paths of compressive members. Thereby, an instability in a single compressive member immediately induces a load increase in adjacent compressed members; with the load transfer becoming more severe each time a member reaches instability. This chain reaction causes the simultaneous localized collapse of a large number of members within a critically oriented plane, resulting in an effective negative stiffness response that leads to catastrophic failure.

As a consequence of delocalized deformation, our tensegrity metamaterials demonstrated unprecedented combination of failure resistance, extreme energy absorption, deformability and strength, outperforming all types of state-of-the-art lightweight architectures including beam-, shell-based and hierarchical designs. Notably, we emphasize that while the plateauing stress–strain response of tensegrity metamaterials resembles that of ideal plastic materials, it is primarily

based on elastic stable buckling and hence reversible. While our experiments were based on micro-scale specimens, finite element simulations showed our findings to be scale-independent. Furthermore, our results are expected to translate from polymer to structural materials like metals, where energy absorption capability over other architectures are expected to increase by several orders of magnitude: higher ratios of Young's modulus to yield strength than the polymer investigated here would allow more slender structures, further increasing elastic energy storage in relation to plastic effects at the lattice nodes. Promising applications for tensegrity metamaterials may range from reusable impact protection systems to large-amplitude vibration isolation devices and adaptive loadbearing structures which efficiently accommodate nonlinear loads and withstand extreme forces via failure-free and reversible large-strain deformation.

We introduced the concept of delocalized deformation as a design paradigm toward superior failure-resistant engineering systems. While we demonstrated tensegrity architecture as one pathway to achieve delocalized deformation, this study may spur widespread future research to explore and abstract delocalization mechanisms and to transfer those to other approaches as well as different structure and material classes, such as continuous solids. Beyond mechanical characteristics, as highlighted in this study, the fundamental benefits of delocalized deformation may thereby reach far across different disciplines.

## Experimental Section

**Fabrication:** All specimens were 3D-printed on fused silica, from the photoresist IP-Dip (Nanoscribe GmbH) using a Photonic Professional GT (Nanoscribe GmbH) two-photon polymerization direct laser writing (TPP-DLW) system operated via fully trajectorial piezoelectric 3-axis stage motion. The TPP-DLW system was equipped with a Plan-Apochromat 63 × 1.4 Oil DIC M27 (Carl Zeiss AG) objective and a FemtoFiber pro NIR (TOPTICA Photonics AG) pulsed laser.<sup>[29]</sup> After TPP-DLW, a 20 min long propylene glycol monomethyl ether acetate (PGMEA) bath dissolved uncured photoresist, followed by a 5 min long isopropanol bath for further cleaning. Specimens were then dried in an Autosamdri-931 (Tousimis Research Corp. Inc.) critical point dryer. Truncated octahedron tensegrity, octet and Kelvin specimens were each composed of 6 × 6 × 6 elementary cells. All specimens were printed with 10 μm s<sup>-1</sup> writing speed, whereby bars were hatched from seven individual print lines. Laser average power and hatching distance between print lines were adjusted between 7.275–8.625 mW and 60–90 nm to create square-shaped bars with equal cross-sectional dimensions for all structures. Relative densities of 4–12% were adjusted via the elementary cell size.

**Experimental Characterization:** Specimen dimensions were optically measured using a FEI Magellan 400XHR (Thermo Fisher Scientific Inc.) SEM. For tensegrity and Kelvin specimens, member cross-section heights of 1047 ± 86 nm and widths of 832 ± 14 nm were measured. Octet member cross-sections were 1113 ± 40 and 847 ± 25 nm high and wide, respectively. Tensegrity specimens with elementary cell sizes of 18.1, 15.4, 13.2, and 10.6 μm had relative densities of ≈4%, 6%, 8%, and 12%, as determined via CAD models. Same density octet structures had elementary cell sizes of 17.8, 14.9, 12.7, and 10.2 μm. Kelvin foam specimens with ≈4%, 8%, and 12% had 12.7, 8.7, and 7.0 μm size elementary cells.

To study the mechanical behavior, uniaxial in situ compression experiments were performed at a constant strain rate of 0.01 s<sup>-1</sup> inside a FEI Quanta 3D FEG (Thermo Fisher Scientific Inc.) dual beam (SEM/FIB), with an Alemnis Nanoindenter (Alemnis AG) equipped with

a 400 μm diameter flat punch diamond tip. Load–displacement curves were recorded and corrected for equipment and substrate compliances using an in-house digital image correlation (DIC) algorithm that tracked specimen tops and bottoms. Applying the measured dimensions, engineering stress and strain were determined. The effective Young's modulus,  $E$ , was extracted as the maximum slope of the linear elastic regime and the yield strength,  $\sigma_y$ , as the 0.2% yield offset relative to  $E$ . The plateau strength,  $\sigma_p$ , was the average stress between 20% and 40% strain.<sup>[30]</sup> If existent, the maximum strength,  $\sigma_m$ , corresponded to the highest stress maximum before failure. The during-deformation absorbed strain energy,  $U$ , was the integral of the stress–strain curves from load onset to densification or failure, whichever occurred first. The densification strain was measured as the global energy absorption efficiency maximum of the corresponding stress–strain curve.<sup>[31]</sup>

The inner specimen deformation distributions were measured via DIC–displacement-tracking of individual lattices node coordinates. Delaunay triangulation of the tracked displacement fields created triangular meshes from which 2D deformation maps of the specimens' front surfaces were interpolated. At a time,  $t$ , local deformation was quantified with the areas  $a_i(t)$ , of the map elements,  $i$ , which were normalized by the initial element areas  $a_i(0)$ . The delocalization efficiency,  $\eta_d$ , which quantifies the resistance against deformation localization was calculated as  $\eta_d = 1 - \frac{\text{std}(a/a_0)}{\text{std}_{\max}(i_t)}$  with the standard deviation,  $\text{std}(a/a_0)$ , of the normalized deformation map element areas,  $a/a_0$ , and the theoretical maximum standard deviation,  $\text{std}_{\max}(i_t) = \frac{r}{2} \sqrt{\frac{i_t}{i_t - 1}}$  where  $r = 1$  was the range of  $a/a_0$ , and  $i_t$  the total number of map elements.

**Computational Characterization:** Finite element analyses of displacement controlled uniaxial compression experiments were performed in ABAQUS (Dassault Systèmes SE) using the modified RIKS method. 6 × 6 × 6 elementary cell tensegrity, octet and iso trusses were constructed from beam elements, which were divided into 13 equal segments. To account for manufacturing imperfections, small sinusoidal pre-deformations equal to 7.5 × 10<sup>-4</sup> % of the bar lengths as well as node offsets equal to 1 × 10<sup>-4</sup> % of the elementary cell sizes were introduced in randomized directions. Corresponding to the experimental tests, top and bottom nodes were fixed in the in-plane directions. All dimensions of the 4%-relative density tensegrity, octet and Kelvin models corresponded to the SEM-measured average values of the experimentally characterized specimens. The 4%-relative density iso truss model had the same bar cross section dimensions as the octet model and the elementary cell adjusted to match the relative density. To create models with relative densities <4%, elementary cell sizes were scaled up relative to the bar cross section dimensions. Parametric optimization of the as-fabricated tensegrity model maximized strength, stiffness and absorbed strain energy while maintaining the same relative density by adjusting the tensile and compressive member cross section edge lengths to 1300 and 450 nm, respectively. Optimized tensegrity models had square shaped cross sections. All simulation were carried out with a nonlinear constituent material model (Figure S5, Supporting Information) representative for the experimentally used polymer IP-Dip.<sup>[32]</sup>

## Supporting Information

Supporting Information is available from the Wiley Online Library or from the author.

## Acknowledgements

J.B., C.C., and L.V. acknowledge support from a NASA Early Stage Innovation program, award No. 80NSSC18K0259, and from the National Science Foundation Division of Civil, Mechanical, and Manufacturing Innovation under grant No. CMMI-1902685. J.R. and J.K.

acknowledge support from the National Science Foundation Division of Civil, Mechanical, and Manufacturing Innovation under grant No. CMMI-1454104.

## Conflict of Interest

The authors declare no conflict of interest.

## Author Contributions

J.B., J.R., and L.V. designed the research. J.B. and C.C. fabricated specimens and conducted experimental characterizations. J.B., C.C., and J.K. analyzed experimental data. J.K. formulated numerical models and carried out finite element analyses. J.B., J.K., C.C., J.R., and L.V. interpreted results and J.B. wrote the manuscript.

## Keywords

delocalized deformation, energy absorption, failure resistance, metamaterial, tensegrity

Received: August 20, 2020

Revised: December 1, 2020

Published online:

- 
- [1] M. F. Ashby, *Philos. Trans. R. Soc., A* **2006**, 364, 15.
- [2] A. G. Evans, M. Y. He, V. S. Deshpande, J. W. Hutchinson, A. J. Jacobsen, W. B. Carter, *Int. J. Impact Eng.* **2010**, 37, 947.
- [3] N. A. Fleck, V. S. Deshpande, M. F. Ashby, *Proc. R. Soc. A* **2010**, 466, 2495.
- [4] J. Bauer, L. R. Meza, T. A. Schaedler, R. Schwaiger, X. Zheng, L. Valdevit, *Adv. Mater.* **2017**, 29, 1701850.
- [5] Z. C. Eckel, C. Zhou, J. H. Martin, A. J. Jacobsen, W. B. Carter, T. A. Schaedler, *Science* **2016**, 351, 58.
- [6] J. Bauer, C. Crook, A. Guell Izard, Z. C. Eckel, N. Ruvalcaba, T. A. Schaedler, L. Valdevit, *Matter* **2019**, 1, 1547.
- [7] L. R. Meza, A. J. Zelhofer, N. Clarke, A. J. Mateos, D. M. Kochmann, J. R. Greer, *Proc. Natl. Acad. Sci. USA* **2015**, 112, 11502.
- [8] X. Zheng, W. Smith, J. Jackson, B. Moran, H. Cui, D. Chen, J. Ye, N. Fang, N. Rodriguez, T. Weisgraber, C. M. Spadaccini, *Nat. Mater.* **2016**, 15, 1100.
- [9] M.-T. Hsieh, B. Endo, Y. Zhang, J. Bauer, L. Valdevit, *J. Mech. Phys. Solids* **2019**, 125, 401.
- [10] J. B. Berger, H. N. G. Wadley, R. M. McMeeking, *Nature* **2017**, 543, 533.
- [11] T. Tancogne-Dejean, M. Diamantopoulou, M. B. Gorji, C. Bonatti, D. Mohr, *Adv. Mater.* **2018**, 30, 1803334.
- [12] J. Bauer, A. Schroer, R. Schwaiger, O. Kraft, *Nat. Mater.* **2016**, 15, 438.
- [13] C. Crook, J. Bauer, A. Guell Izard, C. Santos de Oliveira, J. Martins de Souza e Silva, J. B. Berger, L. Valdevit, *Nat. Commun.* **2020**, 11, 1579.
- [14] L. R. Meza, S. Das, J. R. Greer, *Science* **2014**, 345, 1322.
- [15] A. Schroer, J. M. Wheeler, R. Schwaiger, *J. Mater. Res.* **2018**, 33, 274.
- [16] A. Guell Izard, J. Bauer, C. Crook, V. Turlo, L. Valdevit, *Small* **2019**, 15, 1903834.
- [17] C. M. Portela, A. Vidyasagar, S. Krödel, T. Weissenbach, D. W. Yee, J. R. Greer, D. M. Kochmann, *Proc. Natl. Acad. Sci. USA* **2020**, 117, 5686.
- [18] S. C. Han, J. W. Lee, K. Kang, *Adv. Mater.* **2015**, 27, 5506.
- [19] L. Dong, V. Deshpande, H. Wadley, *Int. J. Solids Struct.* **2015**, 60, 107.
- [20] T. A. Schaedler, A. J. Jacobsen, A. Torrents, A. E. Sorensen, J. Lian, J. R. Greer, L. Valdevit, W. B. Carter, *Science* **2011**, 334, 962.
- [21] H. Söker, in *Advances in Wind Turbine Blade Design and Materials*, Elsevier Inc., New York **2013**, pp. 29–58.
- [22] R. B. Fuller, *US3063521 A*, **1962**.
- [23] A. Pugh, *An Introduction to Tensegrity*, University of California Press, Berkeley, CA, USA **1976**.
- [24] D. E. Ingber, *J. Cell Sci.* **2003**, 116, 1157.
- [25] K. Caluwaerts, J. Despraz, A. İççen, A. P. Sabelhaus, J. Bruce, B. Schrauwen, V. SunSpiral, *J. R. Soc., Interface* **2014**, 11, 20140520.
- [26] J. J. Rimoli, R. K. Pal, *Compos. Part, B Eng.* **2017**, 115, 30.
- [27] R. E. Skelton, M. C. de Oliveira, *Tensegrity Systems*, Springer Science & Business Media, New York **2009**.
- [28] L. H. Chen, K. Kim, E. Tang, K. Li, R. House, E. L. Zhu, K. Fountain, A. M. Agogino, A. Agogino, V. SunSpiral, E. Jung, *J. Mech. Rob.* **2017**, 9, 025001.
- [29] *Photonic Professional (GT) User Manual*, Nanoscribe GmbH, Eggenstein-Leopoldshafen **2017**.
- [30] M. O. Normalizacyjna, *Mechanical Testing of Metals – Ductility Testing – Compression Test for Porous and Cellular Metals ISO 13314*, ISO, Geneva, Switzerland **2011**.
- [31] Q. M. Li, I. Magkiriadis, J. J. Harrigan, *J. Cell. Plast.* **2006**, 42, 371.
- [32] J. Bauer, A. Guell Izard, Y. Zhang, T. Baldacchini, L. Valdevit, *Adv. Mater. Technol.* **2019**, 4, 1900146.
- [33] D. T. Hashim, F. Hejazi, V. Y. Lei, *Int. J. Concr. Struct. Mater.* **2020**, 14, 1.
- [34] R-Tech Materials, A Practical Guide to Compression Testing of Composites, <https://www.r-techmaterials.com/news-and-blog/practical-guide-compression-testing-composites>, (accessed: August 2020).
- [35] M. D. Uchic, P. A. Shade, D. M. Dimiduk, *Annu. Rev. Mater. Res.* **2009**, 39, 361.
- [36] D. K. Balch, J. G. O'Dwyer, G. R. Davis, C. M. Cady, G. T. Gray, D. C. Dunand, *Mater. Sci. Eng., A* **2005**, 391, 408.
- [37] L. An, J. Wu, Z. Zhang, R. Zhang, *J. Wind Eng. Ind. Aerodyn.* **2018**, 182, 295.
- [38] N. Augenti, F. Parisi, *J. Perform. Constr. Facil.* **2013**, 27, 77.